Droplet Translation Actuated by Photoelectrowetting

Cesar Palma[†] and Robert D. Deegan[*,‡]

†*Applied Physics, University of Michigan, Ann Arbor*

‡*Physics Department and the Center for the Study of Complex Systems, University of Michigan, Ann Arbor*

E-mail: rddeegan@umich.edu

Abstract

In traditional electrowetting-on-dielectric devices droplet are moved about a substrate using electric fields produced by an array of discrete electrodes. Here we show that a drop can be driven across a substrate with a localized light beam by exploiting the photoelectrowetting effect, a light-activated variant of electrowetting-on-dielectric. Droplet transport actuated by photoelectrowetting eliminates the need for electrode arrays and the complexities entailed in their fabrication and control, and offers a new approach for designing lab-on-a-chip applications. We report measurements of the maximum droplet speed as a function of frequency and magnitude of the applied bias, intensity of illumination, volume of the droplet, and viscosity, and introduce a model that reproduces these data.

Introduction

The goal of lab-on-a-chip devices is to perform standard laboratory functions with microliter fluid samples.[1] There are many advantages to such precision technology: lower reagent

usage, faster response times, lower capital equipment investment, compactness, portability and lower overall cost. Moreover, this technology has the potential to usher in a new age of personalized medicine.[2] In order to realize these advantages there are several key scientific and technological challenges to be overcome.

One such issue is the transport of droplets between sites on the chip. Multiple methods are now available to achieve this task. Techniques to transport droplets in devices molded from polydimethylsiloxane (PDMS)[3] are highly developed and widely employed. Pollack *et al.*[4] exploited electrowetting-on-dielectric (EWOD) to transport droplets between electrodes with electric fields. Various passive wicking schemes have been used (*e.g.,* see Carrilho *et al.*[5] for a recent variant). Yeo *et al.*[6] developed a surface acoustic wave technique (SAW) in which droplets are transported on a piezoelectric substrate by waves generated by an array of interdigitated electrodes. Other transport methods include localized heating,[7] optical control of electrowetting,[8–10] and magnetic manipulation.[11]

Some of these techniques rely on a pre-fabricated transport network such as channels in PDMS or hydrophobic patterns on a surface. These approaches have several disadvantages when applied to lab-on-a-chip applications: PDMS devices require external pumps, and the network cannot be easily altered after fabrication, much less *in situ* during an experiment.

Digital microfluidics (DMF)[12,13] platforms based on EWOD[4,14,15] or dielectrophoresis[16,17] circumvents some of these limitations. External pumps are unnecessary since the motion of the fluid is actuated with electric fields. Moreover, the flow can be reprogrammed in situ since the electric fields are generated by discrete electrodes, each of which can be independently activated to steer the fluid. This flexibility entails increased complexity of fabrication and control. Photolithography techniques are necessary to fabricate arrays of discrete electrodes and the interconnection wires needed to address each electrode individually, and multiplexing routines and circuits are necessary to activate the electrodes in the proper sequence.[12] Furthermore, the number of electrodes and the complexity of the hardware and software grow rapidly with the device size. An additional shortcoming of EWOD-type DMF is the

need to match the drops to the electrode size.

Here we demonstrate a new method of droplet transport actuated with light that exploits optical effects in semiconductors. A drop placed on single-crystal moderately doped silicon wafer coated with an insulating film can be laterally moved by shining light on the leading edge of the drop with typical speeds up to 1 cm/s, and sizes ranging 2 - 20 μL (see Fig. 3 and supporting information video). Our method has the advantages of DMF devices without their complexity. The platform is free of moving parts because actuation is achieved by electro-optical means and is superior to devices that require mechanical pumps in terms of portability, maintenance, and time-to-failure. Unlike devices where the fluid is confined to follow a predetermined path, the drops can be moved in any direction at any time. The substrate can also be reused many times, in contrast to devices that actuate via wicking. Our technology uses a topographically uniform surface free of electrodes, eliminating the need to employ complex photolithography techniques in fabrication as is required with traditional DMF, SAW or PDMS devices.

Our report is divided into the following sections. It begins with a review of electrowetting and photoelectrowetting. Experimental methods and materials are given next, followed by experimental results. We show that translation of a drop is possible with a voltage-light sequence consisting of (1) a rapidly applied bias that drives the silicon into deep-depletion; (2) illumination that drives the charge distribution beneath one side of the drop into inversion, creating an asymmetry in the charge distribution similar to that achieved in EWOD devices with discrete electrode; (3) zeroing the bias to reset the charge distribution. We also report experimental characterizations of the translational speeds as a function of applied bias, frequency, illumination, viscosity of the fluid, and drop size. Next, we develop a model to account for these dependencies, and compare this model with experiments in the discussion section. We end with a comparison of photoelectrowetting and optoelectrowetting translation, and a discussion of strategies for increasing droplet speeds.

Background

In electrowetting-on-dielectric[18] (Fig. 1a) a potential difference is applied across a droplet of electrolyte and a flat electrical conductor separated by an insulator. The droplet responds by spreading: the contact angle θ decreases and the liquid-solid interface expands. For low voltages the change is well modeled by the Young-Lippmann equation:[19]

$$\cos\theta = \cos\theta_0 + \frac{c}{2\gamma}V^2 \tag{1}$$

where c is the capacitance per unit area of the insulator, V is the applied bias, γ is the liquid-vapor surface tension and θ_0 is the contact angle at zero applied bias. Pollack *et al.*[4] demonstrated bulk fluid motion with EWOD by applying electrical fields asymmetrically with a pattern of electrodes as shown in Fig. 1b.

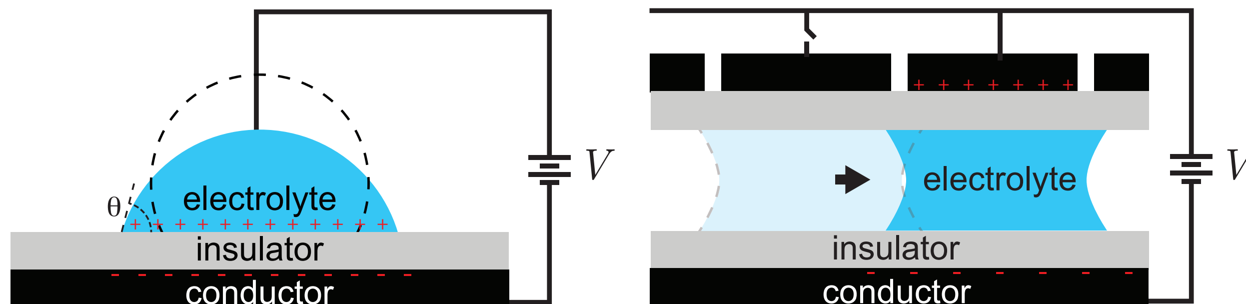

Figure 1: (a) A droplet of electrolyte undergoing a wetting transition in response to applied bias. (b) Droplet motion actuated in DMF device. Dashed lines show the drop prior to the application of the potential. θ indicates the contact angle.

Arscott[20] discovered a new form of EWOD by replacing the metal electrode with a moderately doped crystalline silicon wafer. As with a metal electrode, a drop on a silicon electrode spreads following the application of a voltage bias. Unlike on a metal electrode, subsequent illumination induces a second spreading event. These processes are illustrated schematically in Fig. 2. Arscott called this additional spreading *photoelectrowetting* (PEW).[20–22]

As noted by Arscott,[20] the liquid-insulator-semiconductor stack resembles the well-known metal-oxide-semiconductor (MOS) capacitor. Palma & Deegan[23] showed that photoelec-

trowetting is due to the equilibration of the charge distribution within the semiconductor from a long-lived non-equilibrium state (see Fig. 2) characteristic of MOS capacitors. MOS capacitors exhibit different charge distributions known as accumulation, deep-depletion and inversion.[24] A rapidly applied large DC bias (negative for n-type, positive for p-type) between the electrolyte and the semiconductor produces an initial spreading of the droplet and drives the semiconductor into a long-lived metastable electronic state, *deep-depletion*. The deep-depletion state decays slowly towards the equilibrium state, *inversion*, by the thermal generation of electron-hole pairs at a rate proportional to the concentration of bulk traps, impurities with mid-gap energy levels; in typical device grade silicon, this decay time is on the order of minutes. Illumination, however, greatly reduces the equilibration time by photo-generation of electron-hole pairs (see *e.g.,* Sze[24] or Nicollian and Brews[25]). Thus, illuminating the droplet drives the silicon substrate into inversion, and due to that state's increased charge density the droplet spreads further. Since the transition from deep-depletion to inversion is towards thermodynamic equilibrium, the transition is irreversible and removing the light has no effect. Palma & Deegan[23] showed that Eq. 1 must be replaced by a more complicated form that accounts for the penetration of the electric field into the semiconductor.

Previous work on PEW[20–23,26,27] focused on spreading in which the center of mass of the droplet remains static. Here we show for the first time that PEW can also be used to move the center of mass of the drop by a combination of voltage cycling and partial illumination of the drop.

Experimental methods and materials

Substrate

Photo-electrowetting devices were constructed from n-type (phosphorus) 4" silicon wafers (Silicon Valley Microelectronics) with a resistivity $\rho = 2.93$ ohm-cm (measured with a four-

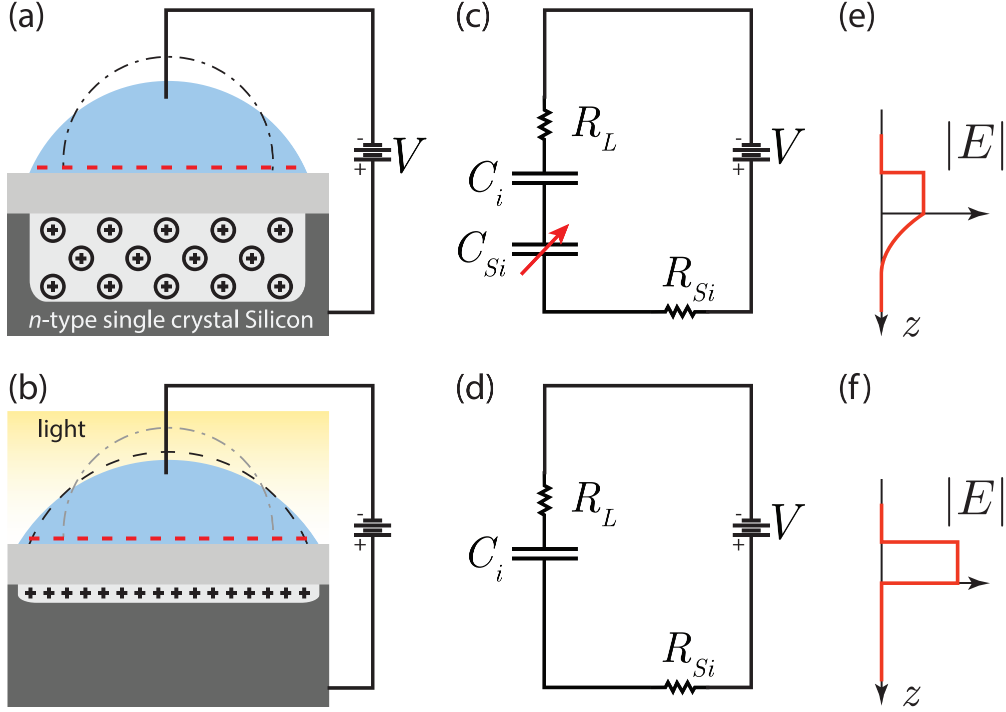

Figure 2: Photoelectrowetting effect for an n-type device. (a) Applying a potential difference between the drop and the silicon induces spreading from the initial state (dashed line), and generates a deep depletion layer in the silicon. The circled + indicate immobile ionized dopants and the - indicate electrons. (b) Subsequent illumination generates mobile electron-hole pairs (holes depicted with +) that replace the depletion layer with an inversion layer, and cause further spreading. ((c) & (d)) Equivalent lumped circuit diagrams and ((e) & (f)) electric fields as a function of depth corresponding to (a) & (b), respectively. Subscripts in (c) & (d) correspond to liquid (L), silicon (Si), and insulator (i). Note that the absence of C_{Si} from (d) indicating the ejection of the electric field from the silicon.

probe technique) and a dopant concentration $N = 1.58 \times 10^{15}$ cm^{-3} estimated from the resistivity.[24] A 100 nm SiO_2 layer was grown on the wafer by dry oxidation at 1000° C for 125 minutes in an oxygen atmosphere containing trans 1,2-dichloroethylene, added to neutralize mobile ionic charges in the oxide, followed by a 10 minute anneal in a nitrogen atmosphere. Two ohmic contact were formed on the backside of the wafer by removing the grown oxide from the target areas with a diamond scribe, depositing a 1.5 μm aluminum layer on the now bare silicon by physical vapor deposition, and annealing at 500° C for 5 minutes in an argon atmosphere. Current measurements between the contacts were used to verified that the contacts were free of rectification effects.[24] Lastly, a teflon film was deposited on

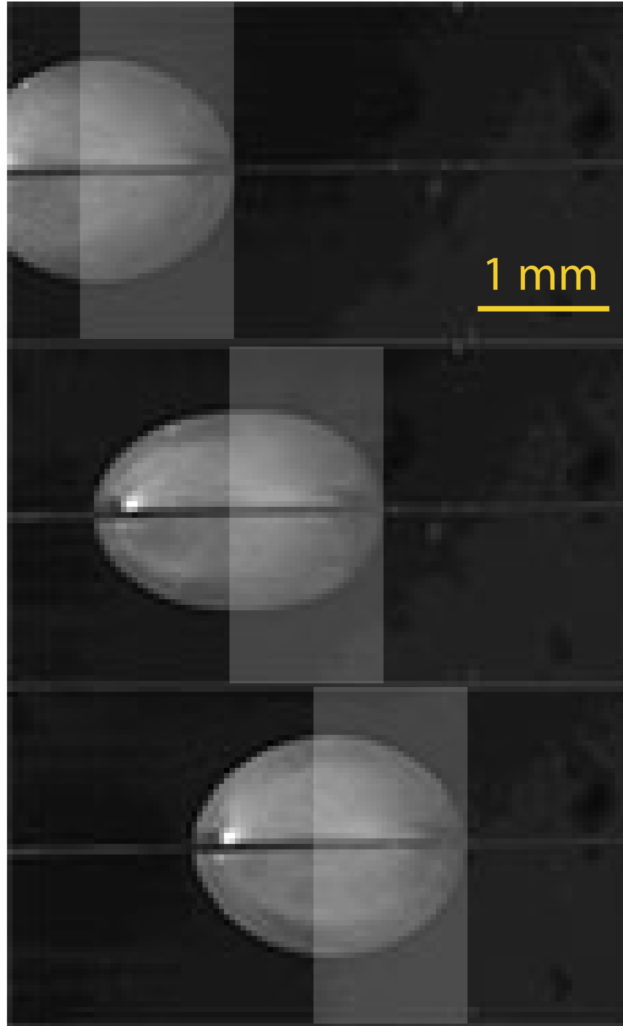

Figure 3: Sequential images of droplet motion actuated by photoelectrowetting. Pictures 1 sec apart. The laser line has been optically filtered out to prevent excessive glint; the lightened patches depict the position of the line. Microscopic particles were added to the fluid to enhance drop visibility.

top of the oxide by spin coating a 2% (w/w) solution of teflon AF1600 (DuPont) in FC-40 (Sigma-Aldrich) for 20 seconds at 500 rpm followed by 30 seconds at 1000 rpm. The film was annealed in an N_2 atmosphere at 1 atm for 15 minutes at 183° C followed by 15 minutes at 330° C. The resulting teflon film was 265 nm thick. The measured capacitance per unit area of these insulating layers was $5.4 \times 10^{-5}\,\mathrm{F/m^{-2}}$, in good agreement with the value expected from the relative permittivities (3.9 for silicon [24] and 1.92 for AF 1600 teflon [20]). The oxidation and ohmic contact deposition steps were performed in a class 100 cleanroom

and the teflon deposition in a class 1000 cleanroom. The SiO_2 layer was added to improve the dielectric strength and remove interface traps and ionic charges, teflon was added on top of the SiO_2 to make the surface hydrophobic, and the film thicknesses were chosen as a compromise between maximizing the capacitance while maintaining the dielectric strength of the film.

Electrolyte solution

An aqueous NaCl solution (1% w/w) with sodium dodecyl sulfate (SDS) (5 mM) was used in all but the viscosity experiments. The surfactant SDS reduces surface tension, thus increasing the change of contact angle obtained for a given voltage level (*e.g.,* Eq. 1). A water-glycerol mixtures (0%, 29%, 40% and 48 % (w/w)) with acetic acid (1.0 M) and SDS (10 mM) was used in experiments where the viscosity was varied.

Light source and beam steering

A 660nm laser (StockerYale Lasiris PureBeam) with variable output up to 50 mW was used in all measurements. The beam was focused by a line generating optic into a fan-shaped light sheet with 95% of the power localized within a line 1.4 mm wide and 7 cm long at 35 cm from the optic. The position of the laser line was controlled with a pair of mirrors mounted on computer controlled galvanometers (Thorlabs GVS002).

Experimental Results

As shown in Fig. 3 and in the supporting information video, we successfully translated droplets across the substrate using PEW. The drop speed was measured for a single droplet with a volume in the range 2 - 20 μL. The solution was pipetted onto the teflon coated surface and the resulting drop bridged the gap between the surface and a stainless steel wire positioned approximately 2 mm above the surface as illustrated in Fig. 4. A typical

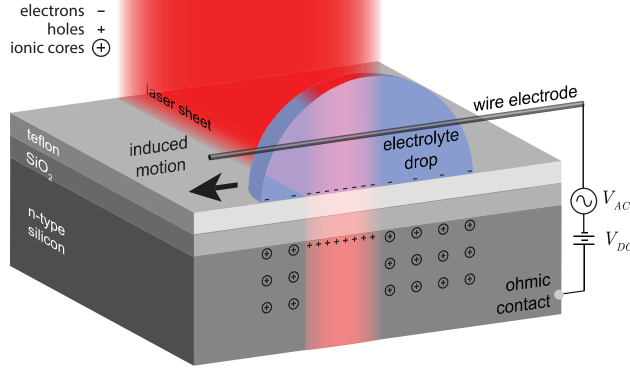

Figure 4: Experimental apparatus for observing drop translation with photo-electrowetting. The substrate consists of a silicon wafer topped with an oxide and a teflon film. A straight stainless steel wire runs parallel to the substrate approximately 2 mm from the surface, and a drop of electrolyte bridges the gap between the wire and surface. A voltage is applied between the wire and an ohmic contact on the silicon. A negative bias produces a deep depletion layer in the silicon where it is dark and an inversion layer where it is lit.

10 μL drop had a static contact angle $\theta \approx 85^o$ and a solid/liquid contact area with radius $R \approx 2.5$ mm. A sinusoidal potential difference with an offset was applied between the wire and silicon ohmic contact: $V_{DC} + V_{AC} \sin(2\pi f t)$ where t is time. The AC bias V_{AC} was limited to less than 35 V in order to remain well below the threshold for dielectric breakdown ($\approx$ 80 V), the offset V_{DC} was kept at -7 V throughout our experiments, and the frequency f was varied between 1 and 1000 kHz. While not essential, the offset increases the average force on the drop, as will be shown below. A laser sheet with a constant and continuous power output was swept with a fixed speed in a direction perpendicular to the plane of the sheet. At low sweep speeds the advancing edge of the drop moved with the laser: the distance between the edge of the drop and the center of the laser beam remained constant. As the sweep speed increased, the distance between the laser beam center and the edge diminished, and at a certain speed, we call the maximum speed u, the drop is just able to keep pace with the laser.

We characterized this motion by measuring the maximum speed as a function of frequency, light intensity I, AC bias, viscosity and drop radius. These data are shown in Figs. 5 and 6. There is a frequency window in the speed versus frequency data (Fig. 5(a))

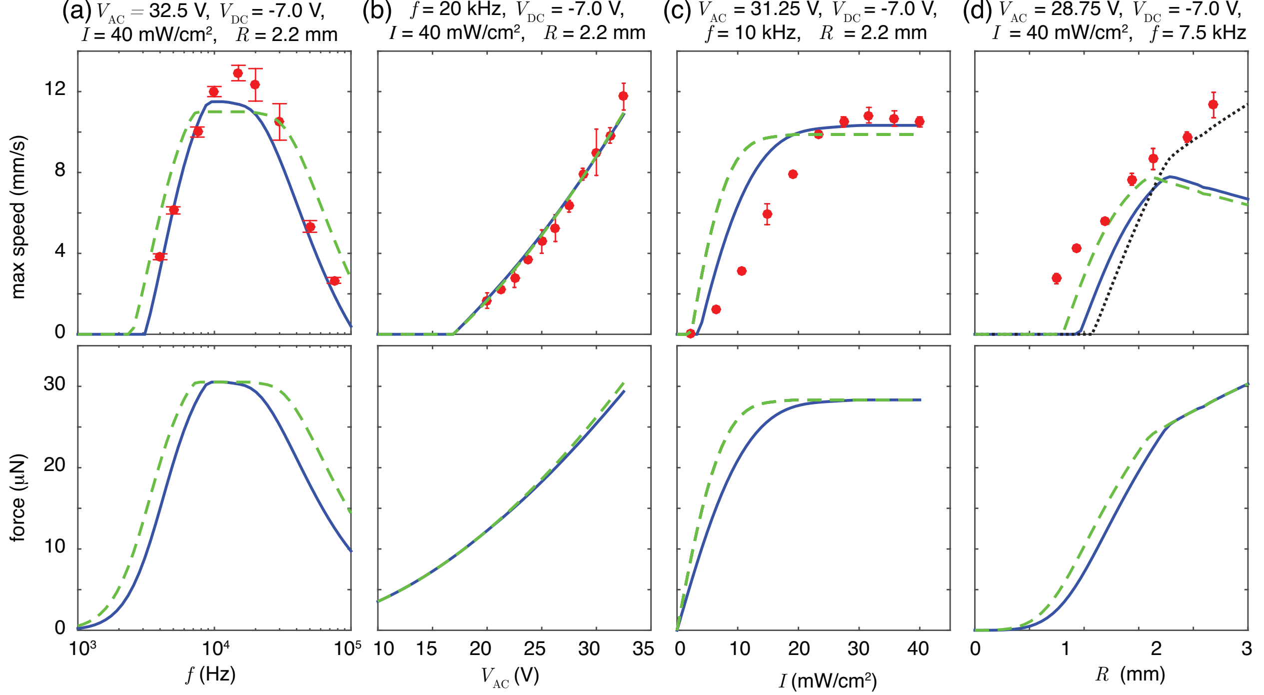

Figure 5: From left to right: Maximum drop speed u (top) and maximum force $\bar{F}$ (bottom) versus (a) frequency f, (b) voltage amplitude V_{AC}, (c) light intensity I, (d) radius of liquid-solid interface R. All data are for water droplets with NaCl (1 % w/w) and SDS (5 mM). The red circles are measurements, and the error bars indicate plus or minus one standard deviation. The green dashed lines in the force plots are calculations from our model for the measured parameters. The solid blue lines are for the same model with the parameters tuned as described in the text to give a better fit to the speed data. The speed is computed from the force assuming that $u = \xi(\bar{F} - F_p)$ where ξ is an effective mobility and F_p is a pinning force determined by fitting to the data in (b). The values of ξ and F_p are rescaled in (d) to account for their dependence on R yielding the green and blue curve; the black curve shows the speed obtained from the green force curve without rescaling ξ and F_p.

centered around 14 kHz where the translation speed of droplets is maximum. As might be anticipated, the speed increases for larger drives (applied voltage; Fig. 5(b)) and decreases with greater resistance (viscosity; Fig. 6). The speed increases for larger drop sizes (Fig. 5(d)) and stronger illumination (Fig. 5(c)), though with the latter, the speed levels off around $I = 40\,\mathrm{mW/cm^2}$. Extrapolating these data to zero speed yields thresholds for motion of 17 V for the AC bias and 250 μm for the radii, equivalent to 20 nl drops.

Our model (see below) incorporates two effects to account for the frequency window in Fig. 5(a): on long timescales (low frequencies) minority carrier migrate away from the lit

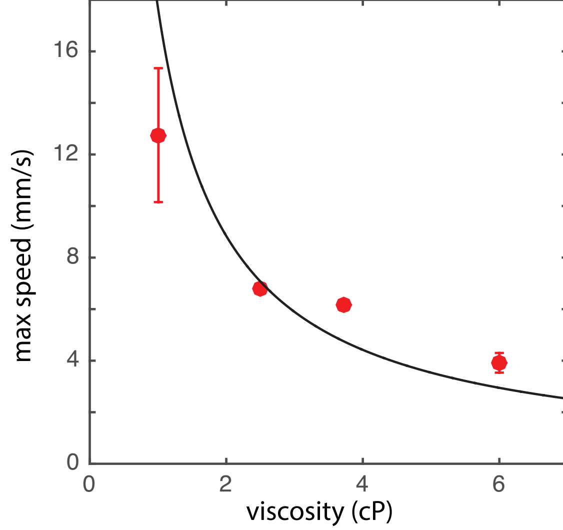

Figure 6: Maximum drop speed u versus dynamic viscosity η at $f = 20\,\text{kHz}$, $V_{AC} = 27.5\,\text{V}$, $V_{DC} = -7\,\text{V}$, and $I = 40\,\text{mW/cm}^2$ for 10 μL droplet of an acetic acid (1.0 M) solution in water with a surfactant (10 mM SDS) and varying glycerol concentrations. The black curve is a fit to $u = A/\eta$ that yields $A = 17.6\,\text{cP mm/s}$.

region, where they form, to dark regions, and at high frequencies the number of incident photons per cycle decreases. We experimentally measured the onset of these effects.

We measured the contact angle as function of frequency for a static drop both in the dark and with uniform illumination. The apparatus was the same as used in the speed measurements, except that the laser line was oriented parallel to the wire so that both edges of the drop were simultaneously lit. These data (Fig. 7) show that the dark contact angle is constant ($\approx 67^o$) up to the highest measured frequency. The lit contact angle is also constant ($\approx 57^o$) up to around 25 kHz, but thereafter rises with frequency until by around 100 kHz the lit value equals the dark value.* Thus, the effect of illumination wanes above 25 kHz. Since the force varies with the difference in contact angle, the diminishing effect of illumination is consistent with high frequency tail in Fig. 5(a).

We measured the migration time of minority carriers (holes for our n-type silicon) from the electrical response of an MIS capacitor to light. A schematic of the experiment is shown

*The absence of frequency dependence in the dark values indicates that the increase in the lit values is intrinsic to the semiconductor, and cannot be ascribed to extraneous effects such as conductivity of the electrolyte or impedance of the circuit.

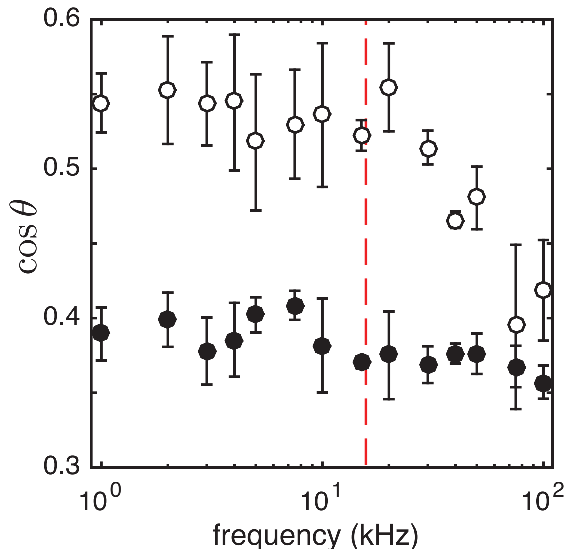

Figure 7: Cosine of the advancing contact angle $\cos\theta$ versus frequency of applied bias V_{AC} with (○) and without (•) illumination for $V_{AC} = 32.5\,\mathrm{V}$, $V_{DC} = -7\,\mathrm{V}$, and $I = 40\,\mathrm{mW/cm^2}$. The dashed red line shows the theoretical frequency threshold f_c. Droplets were 10 μL of a solution of NaCl (1% w/w) with a surfactant (5 mM SDS).

in Fig. 8. A circular semitransparent gold electrode[28] was deposited on the upper surface of a teflon/oxide coated wafer. The electrode was 205 Å thick with a 1.0 mm radius. A DC potential was applied between the electrode and the ohmic contact, and then part of the electrode was illuminated with a laser sheet, creating minority carriers in that area. The migration of minority carriers to the unlit area produces a current in the external circuit, consisting of a $1\,\mathrm{k\Omega}$ resistor in series with the gold-insulator-silicon capacitor (see setup in Fig. 8), that was measured with an oscilloscope from the potential drop across the resistor. The laser sheet was 1.4 mm wide and its intensity on the electrode was $500\,\mathrm{mW/cm^2}$, chosen such that after attenuation by the gold layer the intensity impinging on the silicon surface approximated the intensities in the experiments with drops. We define the migration time τ as the time needed for the current to vanish.

Current signals from two measurements are shown in Fig. 8(c). τ increases monotonically with distance from the farthest edge. The migration times for multiple distances are shown in Fig. 9. A fit to the data shows that the migration time grows as the distance to the farthest

edge squared with a prefactor $1/D$ where $D = (1.4 \pm 0.1) \times 10^3\,\mathrm{cm}^2/\mathrm{s}$. The migration time for a drop with $R = 2\,\mathrm{mm}$ is $\tau = 116\,\mu\mathrm{s}$, corresponding to $f = 1/(2\tau) = 4.3\,\mathrm{kHz}^\dagger$, consistent with the low frequency tail in Fig. 5(a).

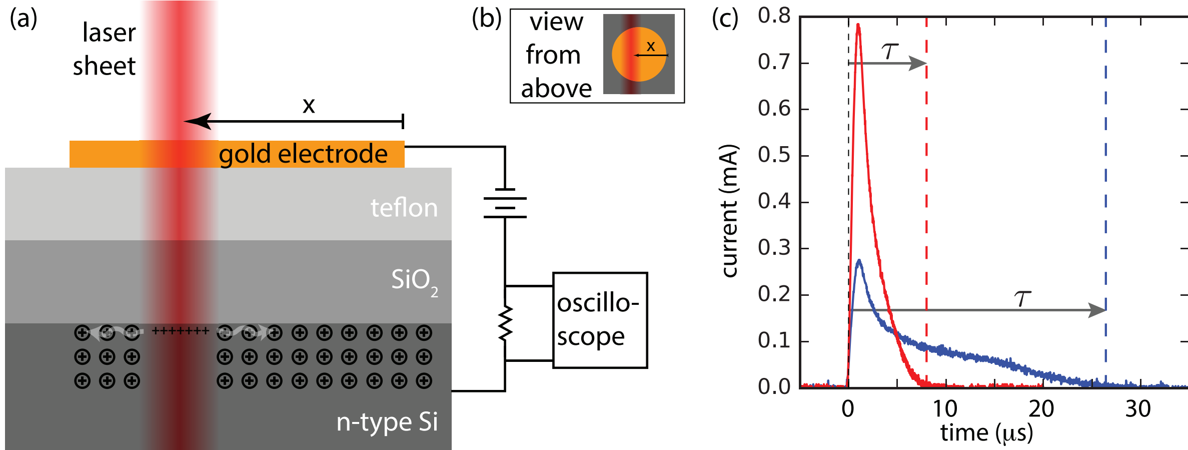

Figure 8: (a) Schematic of migration time experiment. A laser sheet generates electron-hole pairs along its path. The electrons recombine with the ionic charges and the holes are driven to the surface very quickly. On a much longer timescale the holes on the surface migrate laterally into the non-illuminated areas, inducing a current in the external circuit that only ends when the charge distribution is uniform. Since the RC-constant of the external circuit is less than 500 ns, it does not affect the data in (c). The peak intensity of the laser line was $500\,\mathrm{mW/cm}^2$. (b) Top view of (a). (c) Current versus time following illumination of a gold-telfon-oxide-silicon capacitor with a laser sheet striking the gold electrode close to the edge (blue) and in the center (red). The migration time τ denotes the time for the minority carriers to reach the farthest edge of the capacitor.

Model

Reviewing the physics of spreading by PEW, as illustrated in Fig. 2, is a useful starting point for describing our model of translation. As shown in Palma and Deegan,[23] the charge distribution in the silicon beneath the drop is in deep depletion for a negative bias:‡ the electric field penetrates the silicon (see Fig. 2(b)) because the only available screening charges are immobile ionized donors. This configuration is metastable, and it is driven into equilibrium

†The factor of two comes from equating the half-period with the migration time

‡The same is true for a p-type device with all the signs reversed.

when exposed to above-bandgap illumination. Absorbed photons create electron-hole pairs, the electrons recombine with the ionized donors, and the holes migrate to oxide-silicon interface, ejecting the electric field (see Fig. 2(a)). The reconfiguration of the electric field changes the balance of surface and electrostatic energy, and as a result the drop spreads.

Spreading experiments were done with spatially uniform illumination, whereas the drop translation experiments reported here were done with localized illumination. As the voltage oscillates the charge configuration in the unilluminated areas of the drop alternate between accumulation (positive voltage) and deep depletion (negative voltage), and the illuminated areas alternate between accumulation (positive voltage) and inversion (negative voltage). Thus, for a negative voltage there is an asymmetry in the charge distribution between the lit and unlit areas that produces a net force on the droplet; for a positive voltage the charge distribution is in accumulation everywhere and there is no net force.

The asymmetry produced during the negative voltage part of the cycle does not develop instantly nor does it necessarily endure the entire half cycle. On short timescales the number of absorbed photons limits the degree of asymmetry. The formation of a complete inversion layer with surface charge cV takes a period of time $cV\varepsilon/(eI)$. Here e is the fundamental unit of charge, and ε is the energy of a photon. Thus, full inversion for a sinusoidally varying bias is achieved only when $f \lesssim f_c$ where $f_c = eI/(2\pi cV\varepsilon)$, and therefore the force on the drop diminishes for frequencies above f_c. This theoretical threshold, indicated by the dashed red line in Fig. 7, agrees well with the frequency threshold observed in the contact angle data. On long timescales the horizontal gradient of the charge distribution relaxes to a uniform distribution by diffusive and electric currents with the timescale τ, and so the force on the drop diminishes for frequencies below $f_\tau = (2\tau)^{-1}$. In summary, there is a frequency window $f_\tau \lesssim f \lesssim f_c$ where the force generated by photoelectrowetting is unaffected by either of these effects and the force is strongest. These effects are illustrated graphically in Fig. 10.

In order to compare with measurements, we calculated the speed of a drop as a function of frequency, AC bias, drop radius, and illumination intensity as follows. First, we calculated

the instantaneous force F on the drop from the Maxwell stress for the field configurations derived in Palma and Deegan[23] (see appendix). This force depends additionally on the width and the position of the laser sheet. The width was set to the experimental value and the position was selected to yield the maximum force because this corresponds to the condition for maximum speed. That the force has a maximum at some fraction of the radius follows from the observation that when the beam is on the center of the drop the force is zero by symmetry, and when the beam is outside the drop the force vanishes.

Second, we averaged the instantaneous force over the entire cycle:

$$\bar{F} = \frac{1}{T}\int_0^{t_e} \mathrm{d}t\; F(t), \qquad\qquad t_e = \min\left\{\frac{1}{2}T, \tau\right\} \tag{2}$$

The time-dependence of F arises from variations of $V(t)$ and the integrated flux of photons. Here T is the period, $1/f$. The migration of minority carriers was modeled by truncating the integral at the time for minority carriers to cross the drop when this exceeds the half period.

Third, we converted the force to speed using the simplest approximation for the drag force $u = \xi(\bar{F} - F_p)$ where F_p is a pinning force and ξ is a mobility. We treated ξ and F_p as parameters, determined by fitting to data for the speed versus AC bias. A least-squares fit yielded $\xi = 0.51\,\mathrm{mm/s}/\mu\mathrm{N}$ and $F_p = 9\,\mu\mathrm{N}$. These are consistent with literature values; for example Le Grand *et al.*[29] found for $6\,\mu$L droplets of 10 cP silicone oil on an inclined plane $\xi = 0.37\,\mathrm{mm/s}/\mu\mathrm{N}$ and $F_p = 6.1\,\mu\mathrm{N}$. The R-dependence of the speed was computed by rescaling these values based on the theory of contact line dynamics:[30] $\xi \to \frac{R}{R_o}\xi$ and $F_p \to \frac{R}{R_o}F_p$ where $R_o = 2.2\,\mathrm{mm}$ is the radius of the drop used in the AC bias dataset from which ξ and F_p were extracted.

Discussion

Comparison of experiments with the model

The green dashed line in the bottom panels of Fig. 5 shows the force curves computed from our model. In this computation, all the parameters of the model are fixed to the experimentally measured values, *i.e.,* there are no adjustable parameters. These curves show a strong qualitative resemblance to the data for the speeds (upper panels). The speeds calculated from the model are plotted with a green dashed line over the data in the upper panels of Fig. 5. These capture the qualitative features of the data with the exception of the R dependence.

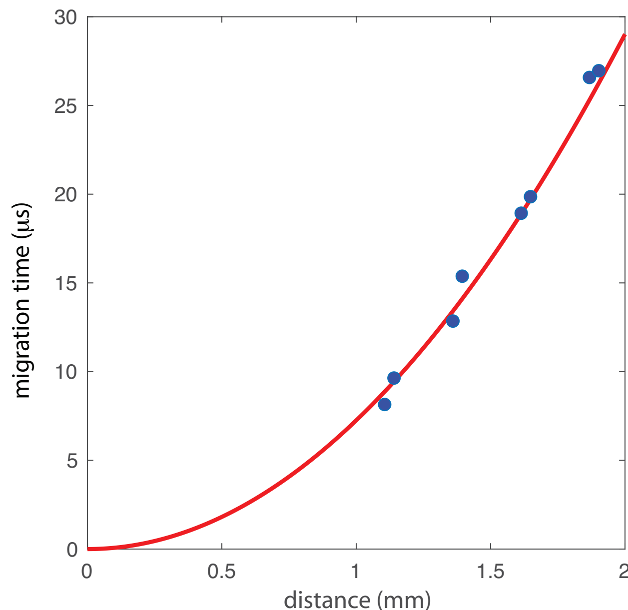

Figure 9: Migration time τ versus distance from the farthest edge determined by the decay time of the current following illumination (see Fig. 8). The line is a fit to a power law with an exponent of 2 that yields a prefactor $7.2 \pm 0.7\,\mu\text{s}/\text{mm}^2$.

There are four potential sources of error that could explain the quantitative deviations of the predicted and measured speed. First, the measured value of I is neither adjusted for the conversion efficiency of photons into electron-hole pairs nor the transmission rate through the liquid and insulator layers. Second, τ is implemented in the model as an abrupt cutoff in

the force (see Eq. 13), whereas the force decays over a finite timescale in the physical device as minority carriers gradually migrate into the dark area. The blue solid curves in Fig. 5 show the improvements possible by varying these two parameters, reducing τ by 20% and I by 45% in the case shown. Third, the linear hydrodynamic speed-force relation may not be quantitatively accurate in our experimental regime because the flows inside the drop have a Reynolds number of 30[§] which is beyond the Stokesian regime in which the theory of contact line dynamics is most developed.[31] Fourth, the aspect ratio of the drop changes when it's in motion (see *e.g.,* Fig. 3) with a magnitude that depends on the volume. Since the length of the contact line depends on aspect ratio, the R-dependence of ξ and F_p is nonlinear.

Comparison of photoelectrowetting and optoelectrowetting

Chiou *et al.*[9] used light to actuate droplet motion on an amorphous silicon substrate. They observed droplet motion in response to the instantaneous application of an AC bias and above-bandgap illumination that they termed optoelectrowetting (OEW). They model this phenomenon with Eq. 1 in which V is replaced by the root-mean-squared voltage across the insulator layer. In their model light decreases the resistance of the photo-conductive layer, increasing the root-mean-squared voltage across the insulator.

Optoelectrowetting and photoelectrowetting achieve the same results – actuation of droplet motion without arrays of electrodes – but are different phenomena. The most apparent difference is that OEW operates by regulating the resistance of the semiconductor, whereas PEW regulates the capacitance. Moreover, in contrast to photoelectrowetting which relies on a non-equilibrium metastable state (deep depletion), optoelectrowetting relies on near equilibrium states. The difference is most notable in the low and high frequency limits. Optoelectrowetting in these limits vanishes because the impedance difference between the lit and dark regions is dominated by components unaffected by light. Photoelectrowetting also vanishes in these limits but due to relaxation of the non-equilibrium state at low frequencies

[§]For $v = 15\,\mathrm{mm/s}$, density $1\,\mathrm{g/cm^3}$, $\eta = 1$ cP, and a length scale of $2\,\mathrm{mm}$

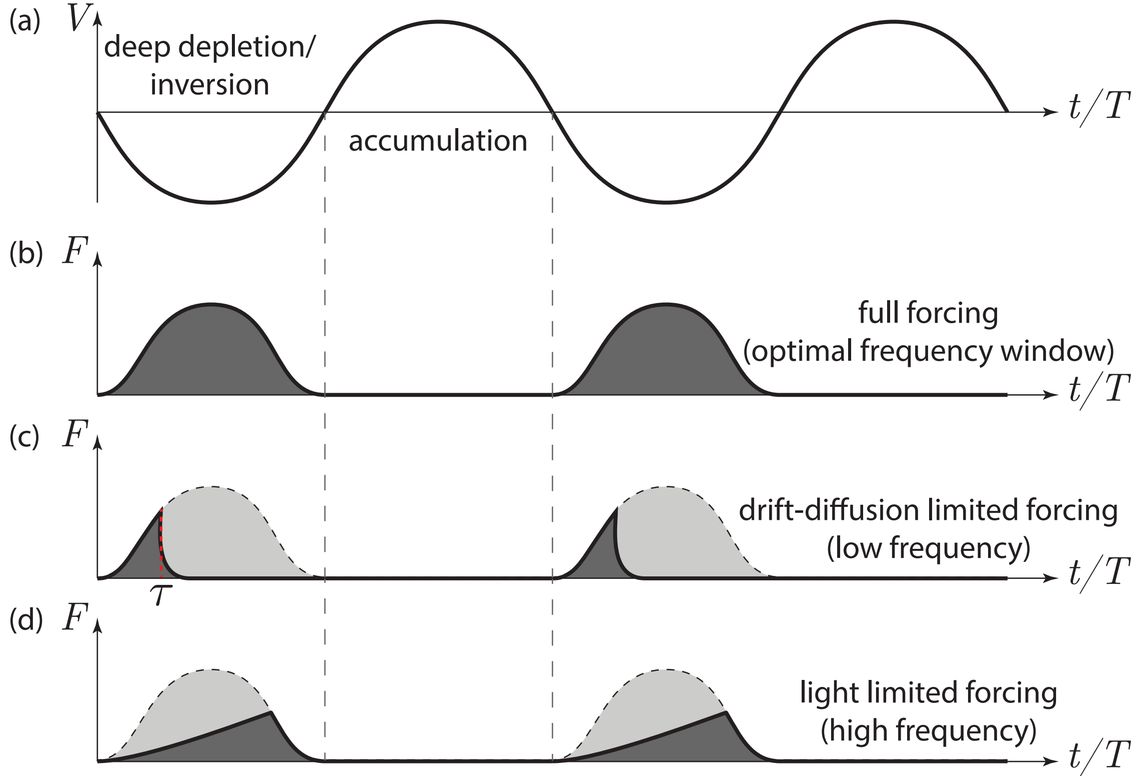

Figure 10: Photoelectrowetting force as a function of time for a sinusoidal voltage applied to an n-type device. (a) For negative voltages the device is partially or fully in inversion where illuminated and in deep depletion elsewhere; for positive voltages the device is in accumulation everywhere regardless of the illumination level. A force is present only while the voltage is negative because only then can the charge distribution be asymmetric. (b) For frequencies within the optimal frequency window, the force is active throughout the duration of the negative bias. (c) For low frequencies the duration of the forcing is abbreviated by drift and diffusion of minority carriers across the drop that erodes differences in the charge distribution. (d) For high frequencies the number of photogenerated minority carriers is insufficient to form a complete inversion layer.

and a shortage of photons at high frequencies. Thus, increasing the light power can extend frequency response for photoelectrowetting, but not for OEW.

Another difference stems from the low mobility of carriers in amorphous silicon compared to crystal silicon, a difference of five orders of magnitude for electrons.[24,32] Thus in comparison with photoelectrowetting, the effect of illumination of optoelectrowetting is confined to the illuminated regions of the droplet. As a consequence, optoelectrowetting actuation is easier to apply to smaller droplets.[33] With photoelectrowetting, the time necessary for minority carriers to reach the trailing end of the droplet decreases with smaller droplets,

hence decreasing the actuation force. Our model suggests that this can be mitigated with the use of higher frequencies at the cost of increased electrolyte concentrations, higher laser intensities and/or larger applied biases.

As a practical device, photoelectrowetting has advantages in manufacturability. The devices presented here are easier to fabricate than the equivalent OEW device, especially for a researcher without on-site access to microelectronic fabrication facilities. As noted by Whitesides,[34] ease of fabrication has been a deciding factor in the growing popularity of PDMS microfluidic devices. Most optoelectrowetting devices presented thus far require sophisticated clean room techniques (plasma-enhanced chemical vapor deposition and atomic layer deposition[33]), though a more recent implementation uses spin coating with some success.[35] In contrast, a photoelectrowetting device can be constructed from commercially available pre-oxidized silicon wafers, and teflon can be applied by spin coating or even dip coating.

Optimizing for translational speeds

The speed follows the force, and the maximum force ignoring surface states (see appendix) is

$$F_{max} = R\left[1 - \frac{1}{\alpha^2}\left(\sqrt{1+2\alpha} - 1)\right)^2\right] cV^2 \tag{3}$$

where $\alpha = c^2V/(e\epsilon N)$, ϵ is the permittivity of the semiconductor. Strategies to increase F_{max} include increasing either c or V without exceeding the threshold for dielectric breakdown, or increasing α by selecting a different semiconductor. The easiest route for the latter is to decrease the doping concentration. As N decreases $F_{max} \rightarrow RcV^2$, but the width of the depletion zone increases and may exceed the absorption length of light resulting in less efficient photon capture. Using p-type silicon is unlikely to be beneficial since electron have a higher mobility than holes. An additional strategy, not apparent from Eq. 3, is to increase V_{DC} which effectively increases the fraction of a cycle when the force is non-zero, though this may compromise the resetting of the charge distribution that is essential for deep depletion.

Conclusions

We demonstrated droplet actuation using the photoelectrowetting effect, achieving speeds up to 13 mm/s in microliter sized drops, and measured the dependence of the speed on applied potential, laser intensity, fluid viscosity and droplet size. We introduced a model that accounts for the qualitative features in these data and gives reasonably good quantitative agreement. Our results provide the tools for incorporating photoelectrowetting into microfluidic applications.

Acknowledgement

We grateful for assistance from the staff at the Lurie Nanofabrication Facility at the University of Michigan and for support from DARPA under a Young Faculty Award.

Appendix: computation of force on drop

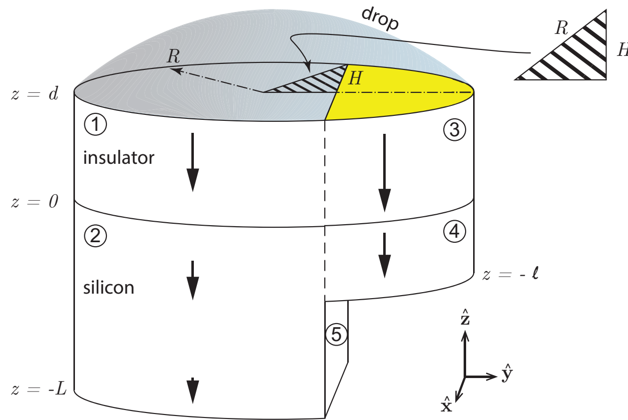

Figure 11: Geometry for computation of Eq. 5.

We divide the drop into dark and lit regions as shown in Fig. 11. The instantaneous force on the drop F lies entirely in the direction of the light gradient ($\hat{\mathbf{y}}$) and is opposite to the force on the dielectric media beneath the drop, *i.e.,* the insulating film and the silicon. We

compute this force from the Maxwell stress σ_{ij}:[36]

$$F = -\oint_S \sigma_{yy} n_y \mathrm{d}S \tag{4}$$

where σ_{yy} is the only contributing component of the Maxwell stress, n_y is y component of the surface normal, and S is the surface enclosing the dielectric and the silicon. We neglect fringe fields and assume the electric field is entirely in the z direction. Surfaces with non-vanishing contributions are labeled $1-5$ in Fig. 11 and yield

$$F = 2H\left[\int_0^d \sigma_{yy}^{(1)}\mathrm{d}z - \int_0^d \sigma_{yy}^{(3)}\mathrm{d}z + \int_{-L}^0 \sigma_{yy}^{(2)}\mathrm{d}z - \int_{-\ell}^0 \sigma_{yy}^{(4)}\mathrm{d}z - \int_{-L}^{-\ell} \sigma_{yy}^{(5)}\mathrm{d}z\right] \tag{5}$$

where H is the half width of the lit area defined in Fig. 11. The electric fields are constant in the insulator film and linear in the silicon (see Palma & Deegan[23])

$$E^{(1)} = E_1 \tag{6}$$

$$E^{(2)} = E_2(1 + z/L) \tag{7}$$

$$E^{(3)} = E_3 \tag{8}$$

$$E^{(4)} = E_4(1 + z/\ell) \tag{9}$$

$$E^{(5)} = E_2(1 + z/L) \tag{10}$$

Continuity of the electric displacement field at the silicon-dielectric boundary and Gauss's law requires:

$$\epsilon_d E_1 = \epsilon_s E_2 = \Sigma_D \tag{11}$$

$$\epsilon_d E_3 = \epsilon_s E_4 = \Sigma_L \tag{12}$$

Here $\Sigma_{L,D}$ are the total charges per unit area in the lit and dark parts of the drop at the liquid-insulator interface, and ϵ_s and ϵ_d are the permittivities of silicon and the dielectric

film.

Using $\sigma_{yy} = -\frac{1}{2}\epsilon E^2$

$$F(t,h) = H\left[\Sigma_L^2\left\{\frac{d}{\epsilon_d}+\frac{\ell}{3\epsilon_s}\right\} - \Sigma_D^2\left\{\frac{d}{\epsilon_d}+\frac{\ell}{\epsilon_s}\left(1-\frac{\ell}{L}+\frac{\ell^2}{3L^2}\right)\right\}\right] \tag{13}$$

where the time and beam position dependence are made explicitly.

The relation between the surface charges and the voltage V were derived in Palma & Deegan:[23]

$$V = \frac{\Sigma_L}{c} + \frac{(\Sigma_L - \sigma - \sigma_s)^2}{2\lambda} \tag{14}$$

$$= \frac{\Sigma_D}{c} + \frac{(\Sigma_D - \sigma_s)^2}{2\lambda} \tag{15}$$

where σ is the minority carrier charge per unit area, σ_s is the surface state charge per unit area, and $\lambda = e\epsilon_s N$ and N is the number of donors per unit volume, e is the fundamental charge unit. The difference between Eq. 14 and 15 is the absence of a minority charge term in the latter, reflecting the absence of minority carriers on the dark side. The values of ℓ and L follow from the zero net charge condition:

$$\Sigma_L = \sigma + \sigma_s + eN\ell \tag{16}$$

$$\Sigma_D = \sigma_s + eNL \tag{17}$$

This completes the specification of the model. As V varies with time, so does F. We find this variation by the following procedure starting from $V = 0$, $\Sigma_{L,D}$=0 at $t = 0$:

1. $V(t) = V_{DC} + V_{AC}\sin 2\pi f(t - t_0)$ where t_0 is selected so that $V(0) = 0$.

2. The surface states charge rapidly and so σ_s follows $\Sigma_{L,D}$ until the surface states saturate at some time t_s determined by the saturation value $e\,G$ where G is the number of surface

states per unit area. During this phase,

$$\Sigma_{L,D} = cV \tag{18}$$

since the second term in Eq. 14 & 15 vanishes, $\ell = 0$, and $L = 0$, and so $F = 0$.

3. Once the surface states are fully charged σ, ℓ, or L can begin to grow.

   - For the lit area σ will follow $\Sigma_L - \sigma_s$ if there is enough light to generate the necessary minority carriers, and if not, it will be limited to the number of photogenerated electrons. For sufficient light $\ell = 0$, $\Sigma_L = cV$; for insufficient light $\sigma = eI(t - t_s)/\varepsilon$ where I is the light intensity and ε is the photon energy, Σ_L is found by solving Eq. 14, and ℓ is given by Eq. 16.
   - For the dark area Σ_D is found by solving Eq. 15, and L is given by Eq. 5.

Results from one such calculation are shown in Fig. 12.

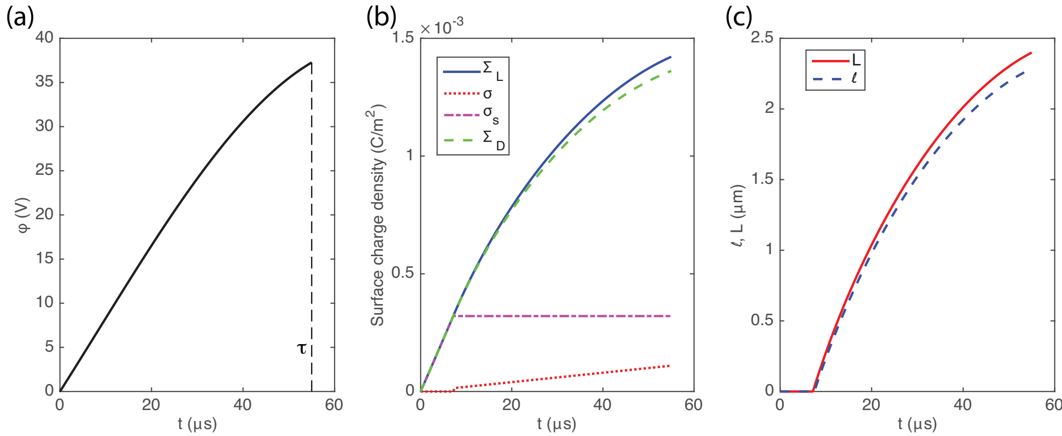

Figure 12: Model input (a) and outputs (b & c).

This algorithm gives the appropriate force when the drop is uniformly lit over a fraction of the area as shown in Fig. 11. However, in our experiments the light sheet illuminates the drop with a gaussian profile with a 1.4 mm width, defined as containing 95% of the power. We approximate this condition as a strip of width $w = 1.4$ mm with constant intensity and

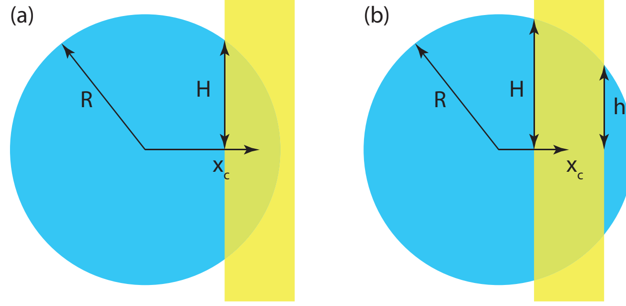

Figure 13: Geometry for different centers of the laser sheet.

the total power equal to that of the beam. Depending on the position of the laser the strip may lie partially inside the drop in which case Eq. 13 is the appropriate form of the force, or it may lie entirely within the drop, flanked by two dark zones in which case a similar calculation shows that Eq. 13 with $H - h$ instead of H is the the appropriate force.

The average force is calculated by averaging the force over whichever is shorter of the time while the bias is negative (*e.g.,* half the period for zero DC bias) or the drift-diffusion time. The resulting force depends on the position of the beam which enters overtly through H and also indirectly through the migration time which varies as the square of the distance between the beam and the far edge of the drop. Since we want to compute the maximum speed, we select the beam position that maximizes the force.

References

(1) Mark, D.; Haeberle, S.; Roth, G.; von Stetten, F.; Zengerle, R. Microfluidic lab-on-a-chip platforms: requirements, characteristics and applications. *Chemical Society Reviews* **2010**, *39*, 1153–1182.

(2) Yager, P.; Edwards, T.; Fu, E.; Helton, K.; Nelson, K.; Tam, M. R.; Weigl, B. H. Microfluidic diagnostic technologies for global public health. *Nature* **2006**, *442*, 412–418.

(3) Duffy, D. C.; McDonald, J. C.; Schueller, O. J.; Whitesides, G. M. Rapid prototyping of microfluidic systems in poly (dimethylsiloxane). *Analytical Chemistry* **1998**, *70*, 4974–4984.

(4) Pollack, M. G.; Fair, R. B.; Shenderov, A. D. Electrowetting-based actuation of liquid droplets for microfluidic applications. *Applied Physics Letters* **2000**, *77*, 1725–1726.

(5) Carrilho, E.; Martinez, A. W.; Whitesides, G. M. Understanding wax printing: a simple micropatterning process for paper-based microfluidics. *Analytical Chemistry* **2009**, *81*, 7091–7095.

(6) Yeo, L. Y.; Friend, J. R. Ultrafast microfluidics using surface acoustic waves. *Biomicrofluidics* **2009**, *3*, 012002.

(7) Darhuber, A.; Valentino, J.; Troian, S.; Wagner, S. Thermocapillary actuation of droplets on chemically patterned surfaces by programmable microheater arrays. *Journal of Microelectromechanical Systems* **2003**, *12*, 873–879.

(8) Chiou, P. Y.; Moon, H.; Toshiyoshi, H.; Kim, C.-J.; Wu, M. C. Light actuation of liquid by optoelectrowetting. *Sensors and Actuators A: Physical* **2003**, *104*, 222–228.

(9) Chiou, P. Y.; Park, S.-Y.; Wu, M. C. Continuous optoelectrowetting for picoliter droplet manipulation. *Applied Physics Letters* **2008**, *93*, 221110.

(10) Chiou, P.-Y.; Chang, Z.; Wu, M. C. Droplet manipulation with light on optoelectrowetting device. *Journal of Microelectromechanical Systems* **2008**, *17*, 133–138.

(11) Zhang, Y.; Nguyen, N.-T. Magnetic digital microfluidics - a review. *Lab Chip* **2017**, *17*, 994–1008.

(12) Abdelgawad, M.; Wheeler, A. R. The digital revolution: a new paradigm for microfluidics. *Advanced Materials* **2009**, *21*, 920–925.

(13) Freire, S. L. S. Perspectives on digital microfluidics. *Sensors and Actuators A: Physical* **2016**, *250*, 15–28.

(14) Cho, S. K.; Moon, H. J.; Kim, C. J. Creating, transporting, cutting, and merging liquid droplets by electrowetting-based actuation for digital microfluidic circuits. *Journal of Microelectromechanical Systems* **2003**, *12*, 70–80.

(15) Lee, J.; Moon, H.; Fowler, J.; Schoellhammer, T.; Kim, C. J. Electrowetting and electrowetting-on-dielectric for microscale liquid handling. *Sensors and Actuators A: Physical* **2002**, *95*, 259–268.

(16) Zheng, L.; Brody, J.; Burke, P. Electronic manipulation of DNA, proteins, and nanoparticles for potential circuit assembly. *Biosensors & Bioelectronics* **2004**, *20*, 606–619.

(17) Fan, S.-K.; Hsieh, T.-H.; Lin, D.-Y. General digital microfluidic platform manipulating dielectric and conductive droplets by dielectrophoresis and electrowetting. *Lab Chip* **2009**, *9*, 1236–1242.

(18) Berge, B. Electrocapillarity and Wetting of Insulator Films By Water. *Comptes Rendus de l'Academie des Sciences Serie II* **1993**, *317*, 157–163.

(19) Mugele, F.; Klingner, A.; Buehrle, J.; Steinhauser, D.; Herminghaus, S. Electrowetting: a convenient way to switchable wettability patterns. *Journal of Physics: Condensed Matter* **2005**, *17*, S559–S576.

(20) Arscott, S. Moving liquids with light: photoelectrowetting on semiconductors. *Scientific Reports* **2011**, *1*, 184.

(21) Arscott, S. Continuous electrowetting at the low concentration electrolyte-insulator-semiconductor junction. *Applied Physics Letters* **2014**, *105*, 231604.

(22) Arscott, S. Electrowetting and semiconductors. *RSC Advances* **2014**, *4*, 29223–29238.

(23) Palma, C.; Deegan, R. D. Electrowetting on semiconductors. *Applied Physics Letters* **2015**, *106*, 014106.

(24) Sze, S.; Ng, K. K. *Physics of Semiconductor Devices*, 2nd ed.; Wiley, 2007.

(25) Nicollian, E. H.; Brews, J. R. *MOS (Metal Oxide Semiconductor) Physics and Technology*; John Wiley & Sons, 1982.

(26) Arscott, S.; Gaudet, M. Electrowetting at a liquid metal-semiconductor junction. *Applied Physics Letters* **2013**, *103*, 074104.

(27) Gaudet, M.; Arscott, S. Optical actuation of microelectromechanical systems using photoelectrowetting. *Applied Physics Letters* **2012**, *100*, 224103.

(28) Axelevitch, A.; Gorenstein, B.; Golan, G. Investigation of optical transmission in thin metal films. *Physics Procedia* **2012**, *32*, 1–13.

(29) Le Grand, N.; Daerr, A.; Limat, L. Shape and motion of drops sliding down an inclined plane. *Journal of Fluid Mechanics* **2005**, *541*, 293–315.

(30) de Gennes, P.-G.; Brochard-Wyart, F.; Quéré, D. *Capillarity and Wetting Phenomena: Drops, Bubbles, Pearls, Waves*; Springer, 2004.

(31) Bonn, D.; Eggers, J.; Indekeu, J.; Meunier, J.; Rolley, E. Wetting and spreading. *Reviews of Modern Physics* **2009**, *81*, 739–805.

(32) Moore, A. Electron and hole drift mobility in amorphous silicon. *Applied Physics Letters* **1977**, *31*, 762–764.

(33) Pei, S. N.; Valley, J. K.; Neale, S. L.; Hsu, H.-Y.; Jamshidi, A.; Wu, M. C. *2010 Conference on Lasers and Electro-optics (CLEO) and Quantum Electronics and Laser Science Conference (QELS)*; 2010.

(34) Whitesides, G. M. The origins and the future of microfluidics. *Nature* **2006**, *442*, 368–373.

(35) Jiang, D.; Park, S.-Y. Light-driven 3D droplet manipulation on flexible optoelectrowetting devices fabricated by a simple spin-coating method. *Lab Chip* **2016**, *16*, 1831–1839.

(36) Mugele, F.; Baret, J.-C. Electrowetting: from basics to applications. *Journal of Physics: Condensed Matter* **2005**, *17*, R705.

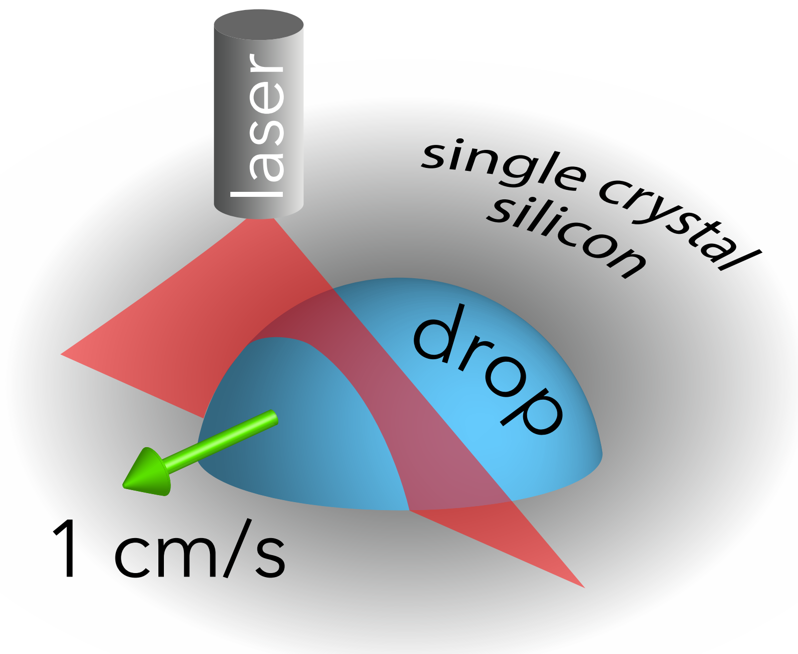
laser
single crystal
silicon
drop
1 cm/s